

Article

Application of Multispectral Sensors Carried on Unmanned Aerial Vehicle (UAV) to Trophic State Mapping of Small Reservoirs: A Case Study of Tain-Pu Reservoir in Kinmen, Taiwan

Tung-Ching Su ^{1,*} and Hung-Ta Chou ²

¹ Department of Civil Engineering and Engineering Management, National Quemoy University, 1 Da Xue Rd., Kinmen 892, Taiwan

² Flying-Aerialphoto Information Co. Ltd., Room 127, CPIC, 151, Yingzhuang Rd., Tamsui Dist., New Taipei City 251, Taiwan; E-Mail: flying.201203@gmail.com

* Author to whom correspondence should be addressed; E-Mail: spcyj@nqu.edu.tw; Tel.: +886-82-313-527; Fax: +886-82-313-528.

Academic Editors: Gonzalo Pajares Martinsanz, Richard Müller, Arko Lucieer and Prasad S. Thenkabail

Received: 16 April 2015 / Accepted: 31 July 2015 / Published: 7 August 2015

Abstract: Multispectral, as well as multi-temporal, satellite images, coupled with measurements, *in situ*, have been widely applied to the water quality monitoring of reservoirs. However, the spatial resolutions of the current multispectral satellite imageries are inadequate for trophic state mapping of small reservoirs which merely cover several hectares. Moreover, the temporal gap between effective satellite imaging and measurements, *in situ*, is usually a few days or weeks; this time lag hampers the establishment of regression models between band ratios and water quality parameters. In this research, the RGB and NIR sensors carried on an unmanned aerial vehicle (UAV) were applied to the trophic state mapping of Tain-Pu reservoir, which is one of the small reservoirs in Kinmen, Taiwan. Due to the limited sampling points and the uncertainty of water fluidity, the average method and the matching pixel-by-pixel (MPP) method were employed to search for the optimal regression models. The experimental results indicate that the MPP method can lead to better regression models than the average method, and the trophic state maps show that the averages of Chl-a, TP, and SD are 179.7 $\mu\text{g L}^{-1}$, 108.4 $\mu\text{g L}^{-1}$, and 1.4 m, respectively.

Keywords: multispectral imagery; unmanned aerial vehicle (UAV); small reservoir; trophic state mapping; matching pixel by pixel (MPP) method

1. Introduction

Reservoirs are important infrastructures of water resource conservation. Periodic water quality monitoring is necessary for water resource sustainability. Traditionally, water quality monitoring is implemented by point-wise measurements, *in situ*, but this approach merely offers water quality conditions for sampling points rather than in regard to the overall reservoir. In order to contribute to the development of an appropriate water quality examination, multispectral satellite sensors, coupled with *in situ* measurement data, have been widely applied to estimate the water quality parameters, such as chlorophyll-a, Secchi disk depth, total phosphorous, turbidity, color, and total nitrogen [1–5], as well as the Carlson trophic state index (TSI) derived from the first three parameters [1].

It has been demonstrated that the multispectral satellite imageries are useful for assisting in the water quality monitoring of the reservoirs [2,6–11]. Based on the Landsat Thematic Mapper (TM) data and *in situ* measurements, Giardino *et al.* [2] built the models with the high determination coefficients to map the chlorophyll concentration and Secchi disk depth throughout the lake. Wang *et al.* [6] presented a method involving radiometric calibration of Landsat-5 TM remote sensors, atmospheric corrections applied to image data, and statistical model construction to find the optimal correlation between reflectance of TM bands and organic pollution measurements. TM3 (red band) and TM4 (near infrared) of Landsat ETM/TM were taken into consideration in calculating the Normalized Ratio Vegetation Index (NRVI), and the regression models between NRVI and chlorophyll-a were built to map the trophic state throughout the reservoir [8]. Bonansea *et al.* [10] considered linear mixed models to determine log-transformed chlorophyll-a concentration and Secchi disk transparency in the R ó Tercero reservoir by using time series Landsat imagery.

Other multispectral data, such as SPOT satellite imageries, were also applied to the water quality monitoring of inland waters [12,13]. Yang *et al.* [12] estimated algal growth and respiration rates by using a one-dimensional water quality model (QUAL2E) and two-dimensional, spatially-distributed water quality data derived from SPOT satellite imagery for the Te-Chi Reservoir in Taiwan. Dekker *et al.* [13] indicated that synoptic information on suspended matter cannot be obtained from an *in situ* monitoring network since suspended matter is a spatially-heterogeneous parameter. Thus, the integrated use of SPOT and Landsat TM sensing data, *in situ* data, and water quality models was proposed to estimate suspended matter concentration in lakes. Recently, medium- to low-resolution satellite imageries, such as Moderate-Resolution Imaging Spectroradiometer (MODIS) and Medium-Resolution Imaging Spectrometer (MERIS), due to their large swath widths and high temporal coverage were well applied to regional-scale measurements of lake water clarity or total suspended matter [14,15]. However, the low spatial resolution of MODIS or MERIS imageries limits the number of lakes that can be assessed [15].

Multispectral satellite imageries have been widely applied to the water quality monitoring of reservoirs, but we think that multispectral satellite imageries could not be applied to map trophic states for the small reservoirs on an appropriate scale. Moreover, the cloud effect and temporal gap between

satellite imaging and measurement, *in situ*, would deteriorate trophic state mappings [16]. Recently, the applications of unmanned aerial vehicles (UAV) for remote sensing are also progressively developing [17–25]. Several applications demonstrated that UAVs carrying multispectral sensors are efficient in environmental monitoring by chlorophyll detection of vegetation. Zarco-Tejada *et al.* [19] used a miniaturized thermal camera and a micro-hyperspectral imager on board a UAV to detect water stress in a citrus orchard. Zarco-Tejada *et al.* [20] also made progress on developing methods for leaf carotenoid content estimation, using high-resolution hyperspectral imagery acquired from a UAV. Torres-Sanchez *et al.* [24] indicated that traditional aerial platforms, such as planes and satellites, are not suitable for these applications due to their low spatial and temporal resolutions. A UAV equipped with a commercial camera (visible spectrum) was used for ultra-high resolution image acquisition over a wheat field in the early-season period. Bendig *et al.* [25] calculated vegetation indices from ground-based hyperspectral data and UAV-based RGB imaging to estimate biomass in a summer barley experiment. Flynn and Chapra [26] used an RGB, wide-angle, digital camera sensor and an off-the-shelf UAV to implement automated classification and mapping of the nuisance green algae *Cladophoraglomerata* in rivers.

For trophic state estimation of reservoirs, this research was proceeded based on the hypothesis that total phosphorous (TP) stimulates growth of algae, *i.e.*, there should be a positive correlation between concentrations of chlorophyll-a (Chl-a) and TP. On the contrary, the higher the concentration of Chl-a, the lower the water transparency. There should be a negative correlation between Chl-a concentration and Secchi disk (SD) depth. We considered that the increasing developments and improvements in unmanned platforms, together with the development of sensing technologies installed onboard such platforms, can offer high versatility and flexibility, as compared to airborne systems or satellites, and can operate rapidly without planned scheduling [27]. This research adopted the RGB and near infrared (NIR) sensors carried on the UAV for the trophic state mapping of one small reservoir in Kinmen.

2. Study Site

Kinmen is located at latitude 24°23′–24°31′N and longitude 118°13′–118°28′E, and covers an area of 150.5 km². Kinmen is administered by Taiwan, but its geographical location is near Xiamen, a city in southeast China. Currently, the small reservoirs covering the areas of 2.5 to 39.3 hectares satisfy the water resource demand in Kinmen, about 13,000 tons per day. Since May 2002, the Environmental Protection Bureau, Kinmen, began to seasonally monitor the water quality parameters for the small reservoirs. Tain-Pu reservoir, one of the small reservoirs, was designed to receive potable water from China in a few years, so it was selected to be the study site (see Figure 1). The reservoir covers an area of 17.8 hectares and has a water capacity of 595,000 m³.

The greater the amount of nutrients (*i.e.*, TP), the more plentiful the phytoplankton, such as algae; as a result, there is less transparency of the water [28]. Algal biomass and water transparency can be roughly estimated by measuring Chl-a concentration and SD depth, respectively. Table 1 summarizes the basic statistics of the measured water quality parameters collected during the measurement, *in situ*, from May 2002 to May 2013. A correlation analysis for the measured water quality parameters is shown in Table 2 and demonstrates that the concentrations of Chl-a or TP would deteriorate Secchi transparency due to the negative Pearson coefficients.

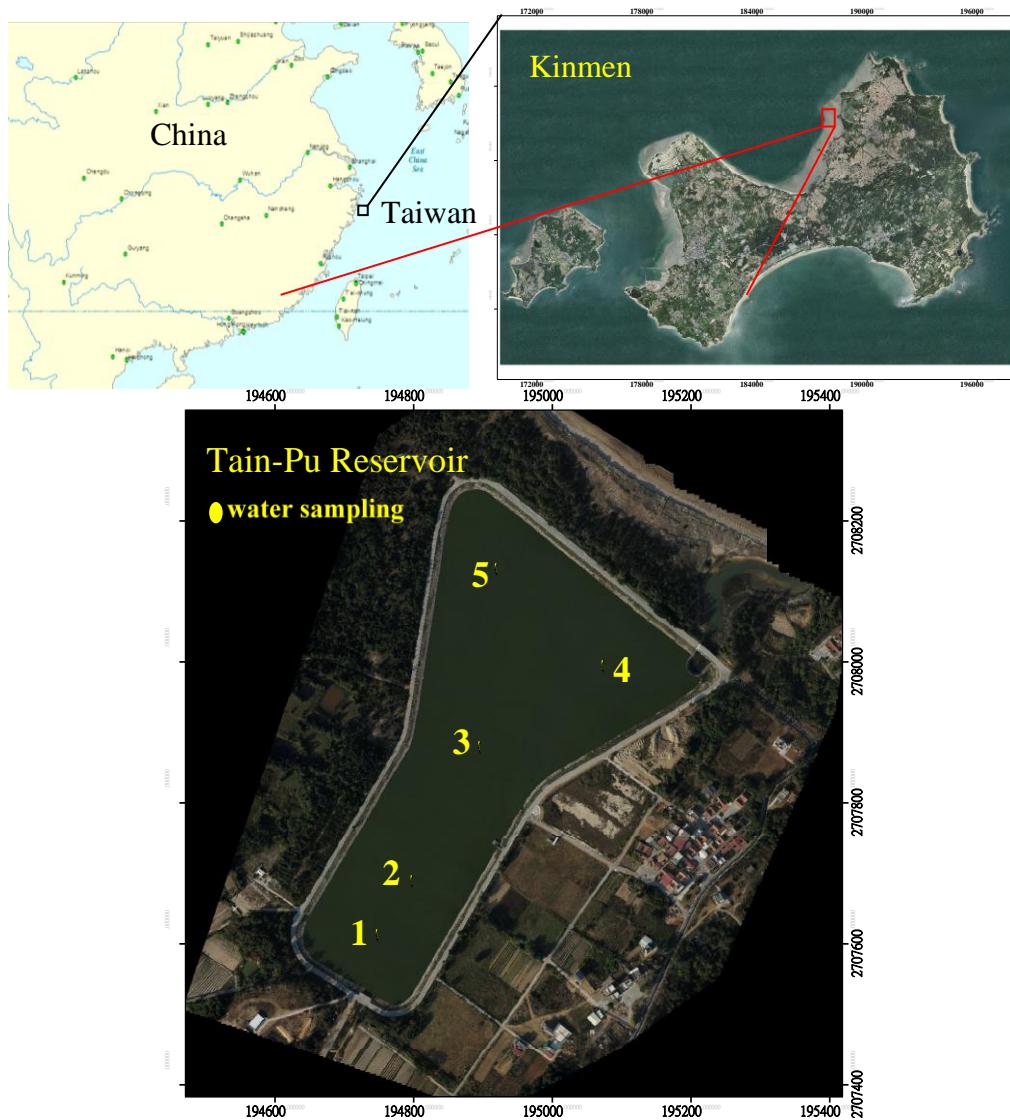


Figure 1. Study site and water sampling points.

Table 1. Range, mean, and standard deviation (Std.) of measured parameters at different climatic seasons of Tain-Pu reservoir during the measurement, *in situ*, from May 2002 to May 2013.

Parameter		Climatic Season			
		Spring	Summer	Fall	Winter
SD (m)	Range	0.1–0.6	0.2–0.8	0.2–0.5	0.1–1.2
	Mean	0.4	0.4	0.4	0.5
	Std.	0.2	0.2	0.1	0.3
Chl-a ($\mu\text{g L}^{-1}$)	Range	24.5–143.0	23.2–124.0	2.4–191.0	12.2–158.0
	Mean	59.0	69.9	75.9	58.0
	Std.	35.8	26.4	61.6	40.4
TP ($\mu\text{g L}^{-1}$)	Range	25.0–126.0	17.9–139.0	18.0–177.0	42.0–121.0
	Mean	57.6	79.9	79.9	76.6
	Std.	25.9	37.4	45.2	29.0

Table 2. Correlation analysis matrix of measured parameters of Tain-Pu reservoir during the measurement, *in situ*, from May 2002 to May 2013.

		SD	Chl-a	TP
SD	<i>r</i>	1	−0.434 **	−0.259
Chl-a	<i>r</i>	−0.434 **	1	0.254
TP	<i>r</i>	−0.259	0.254	1

Notes: 45 samples were involved in the correlation analysis; *r* expresses Pearson coefficient; The *p* values were obtained by two-tail test; ** denotes the significance at the level of 0.01.

3. Methodology

Figure 2 shows the flowchart of applying UAV multispectral imagery, coupled with measurement, *in situ*, to trophic state mapping of small reservoirs. Based on the acquisition of the water quality parameters and the UAV imagery, this research aims to establish the regression models with powerful explanation, where multispectral bands are the independent variables and water quality parameters are the dependent variables. The technical elements of trophic state mapping for small reservoirs are presented as following.

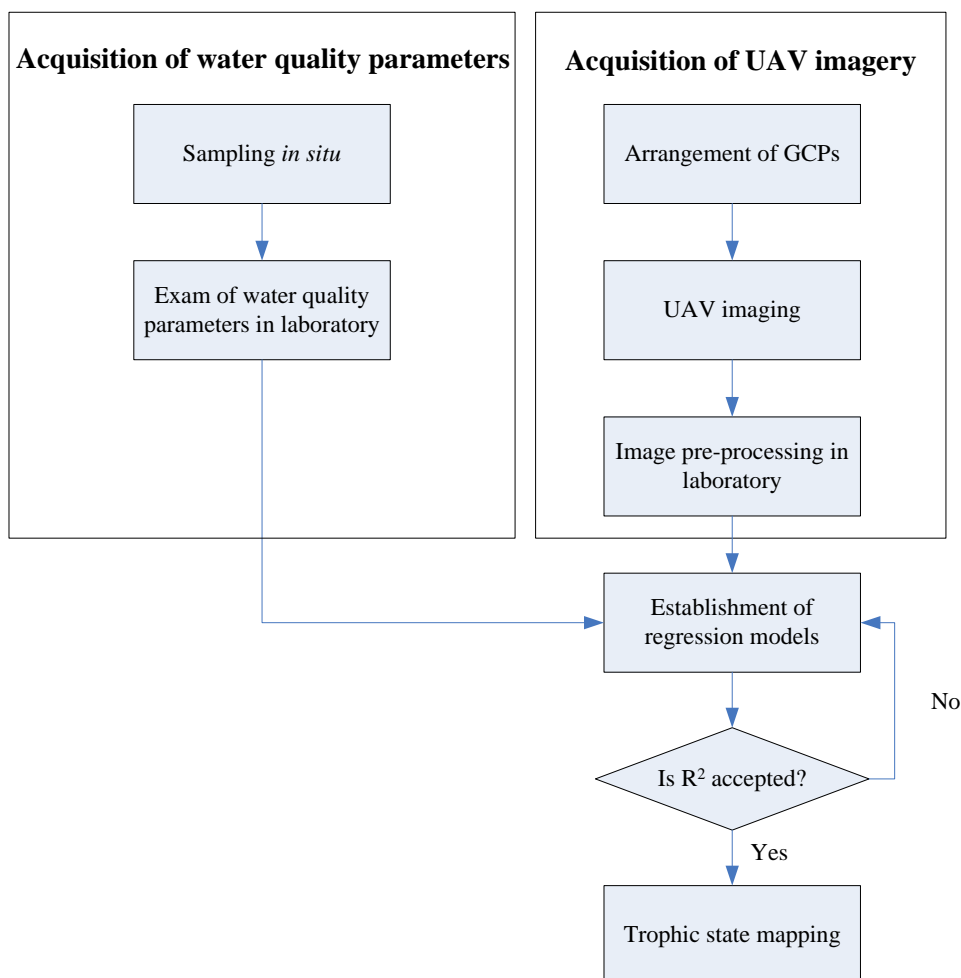


Figure 2.Flowchart of applying UAV multispectral imagery coupled with measurement, *in situ*, to trophic state mapping of small reservoirs.

3.1. Measurement In Situ and Water Quality Exam

On the 24 November 2014, a measurement, *in situ*, coupled with UAV imaging, was implemented for Tain-Pu reservoir. In this research, five sampling points, one measuring data for each sampling point (Figure 1), were prepared for offering the water quality parameters for the establishment of the regression model. Referring to the densities of the sampling points arranged in the range between 0.01 and 2.34 sites/km² [7,8,10,29], the density (five sites in the area of 17.8 hectares = 28.09 sites/km²) of the sampling points in this research is quite sufficient for monitoring such a small reservoir.

The execution of measurement, *in situ*, as well as the water quality examination, was entrusted to SGS, a professional company in testing and certification; the examination results are listed in Table 3. Acetone extraction/spectrophotometer (national standard: NIEA E507.03B), ascorbic acid/spectrophotometer (national standard: NIEA W427.53B), and Secchi disk (national standard: NIEA E220.51C) were used to measure the Chl-a concentration, the TP concentration, and the water transparency, respectively. In NIEA E507.03B, water sampling is filtered by fiberglass, and then 90% acetone is used to extract Chl-a from the fiberglass. Finally, Chl-a concentration is measured by spectrophotometer. In NIEA W427.53B, water sampling is digested by sulfuric acid and peroxydisulfate processes to transform phosphorous into orthophosphate. Phosphomolybdic acid is a product of ammonium molybdate, potassium antimony tartrate, and orthophosphate. Molybdenum blue is a reduction of phosphomolybdic acid by ascorbic acid. Finally, TP concentration is measured by spectrophotometer at 880 nm. In NIEA E220.51C, a white disk of diameter of 20~30 cm, *i.e.*, Secchi disk, is sunk into water to measure visibility from water surface. The details of the above measurement methods can be available from the website of environmental analysis laboratory, EPA, Taiwan [30]. According to the Carlson TSI [31], the trophic class of Tain-Pu reservoir would be eutrophic or hypereutrophic.

Table 3. Examination results of measurement, *in situ*, on 24 November 2014 for Tain-Pu reservoir.

No. of Sampling Point	Water Quality Parameter			Sampling Coordinate (System Name: GCS_TWD_1997)	
	SD (m)	Chl-a ($\mu\text{g L}^{-1}$)	TP ($\mu\text{g L}^{-1}$)	E (m)	N (m)
1	1.8	173.0	105.0	194,750.14	2,707,614.72
2	1.6	185.0	113.0	194,800.16	2,707,690.52
3	2.0	172.0	108.0	194,897.61	2,707,880.43
4	1.5	156.0	99.0	195,075.60	2,707,996.12
5	1.7	177.0	108.0	194,921.69	2,708,132.85

3.2. UAV Multispectral Image Data

A fixed-wing UAV carried the Canon Powershot S110 RGB and NIR sensors to acquire the image data on Tain-Pu reservoir in the visible bands, *i.e.*, blue (B: 0.45 μm), green (G: 0.52 μm), and red (R: 0.66 μm), as well as the NIR band (0.85 μm), respectively (see Figure 3). The technical features of the S110 RGB or the S110 NIR involve resolution of 12 million pixels, a weight of 0.7 kg, ground resolution at 100 m of 3.5 cm/pixel, sensor size of 7.44 \times 5.58 mm², pixel pitch of 1.33 μm , and image format in JPEG. In fact, the image data consisting of the above four bands were acquired by UAV imaging twice. S110 RGB acquired the true-color image data in single UAV imaging; another UAV

imaging with the S110 NIR acquired the false-color image data that consists of green ($0.55\ \mu\text{m}$), red ($0.625\ \mu\text{m}$), and NIR ($0.85\ \mu\text{m}$) bands. In this research, the green ($0.55\ \mu\text{m}$) and red ($0.625\ \mu\text{m}$) bands were abandoned because their responses overlap the green ($0.52\ \mu\text{m}$) and red ($0.66\ \mu\text{m}$) bands.



Figure 3. UAV imagery system: (a) Fixed-wing UAV; (b) RGB (right) and NIR (left) sensors.

3.3. UAV Imaging

The technical features of the fixed-wing UAV, which was produced by senseFly Ltd. in Switzerland and named the eBee, include a wingspan of 96 cm, maximum flight time of 50 min, nominal cruise speed of 40–90 km/h, radio link range of up to 3 km, maximum coverage (single flight) of 12 km², wind resistance of up to 45 km/h, ground sampling distance (GSD) down to 1.5 cm per pixel, relative orthomosaic/3D model accuracy of 1~3 times GSD, and absolute horizontal and vertical accuracies with ground control points (GCPs) down to 3 and 5 cm, respectively. Autopilot continuously analyzes data provided by the inertial measurement unit (IMU) and onboard GPS to control every aspect of the eBee's flight. The integration of the sensors and the UAV with IMU and GPS also enables obtaining direct imaging georeferencing after image processing [27].

The imaging principle of the fixed-wing UAV is similar to that of traditional manned aircraft. In order to orient and relate UAV imagery to the ground, arranging the GCPs is necessary before UAV imaging. Establishing a good control network is extremely important for almost any type of photogrammetric project [32]. In this research, five GCPs and four checking points were arranged around Tain-Pu reservoir in order to obtain photogrammetric imagery with uniform horizontal and vertical accuracy. The proposed locations, style of the GCPs, and checking points are illustrated in Figure 4.

The imaged area of Tain-Pu reservoir, including the surroundings, is about 20 hectares, so that 73 camera stations (single flight) are needed, as shown in Figure 5. The specifications of the UAV imaging comprises ground resolution at 286 m flying altitude of 10 cm/pixel, air base of 60 m, distance between two flight strips of 120 m, swath widths of $400 \times 300\ \text{m}^2$, 80% end, as well as 70% side laps, pixel size of $1.86\ \mu\text{m}$, and focal length of 5 mm. The weather condition in Kinmen was a visibility of 7000 m and a cloud level of 3000 m on 24 November 2014, but the visibility suddenly dropped to 250 m due to heavy fog on 25 November 2014. The UAV demonstrated that its excellent temporal resolution and mobility are helpful for acquiring high-quality remote sensing data. The time needed for a single flight of the UAV imaging for Tain-Pu reservoir is 12 min. Although the locations of the camera stations of the true-color and false-color images are not consistent, image orientation for

navigation and camera calibration can cope with the problem of irregularity of frames acquired from UAV [27]. In the laboratory, we used the Menci Software to retrieve the interior orientation parameters of the S110 sensors. Based on the retrieved interior orientation parameters, coupled with the GCPs, the aerial triangulation provided a geometric correction result with residual error of 0.772 pixels, *i.e.*, ground resolution distance (GRD) of 7.5 cm.

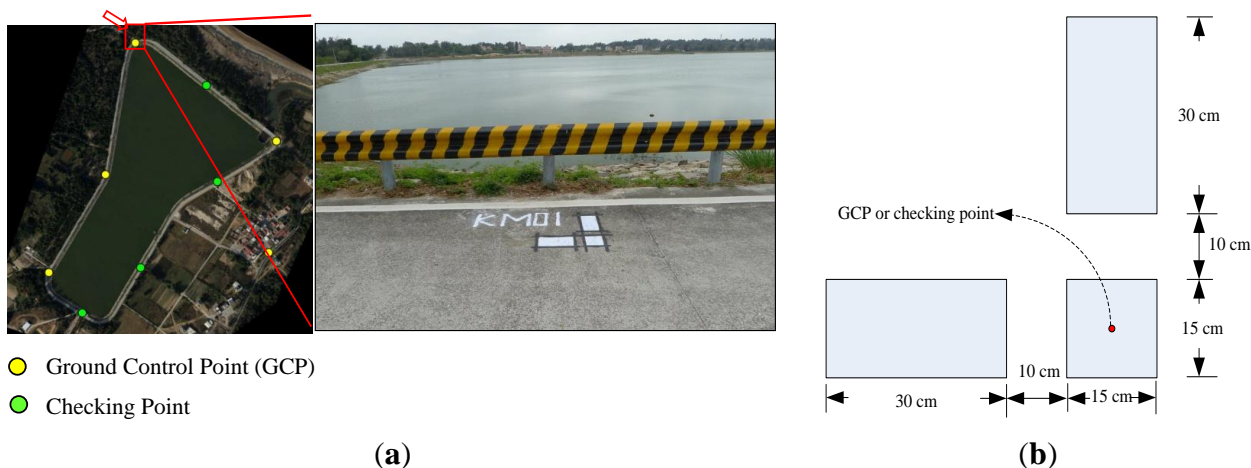


Figure 4. (a) Proposed locations of GCPs and checking points; (b) Style of GCPs or checking points.

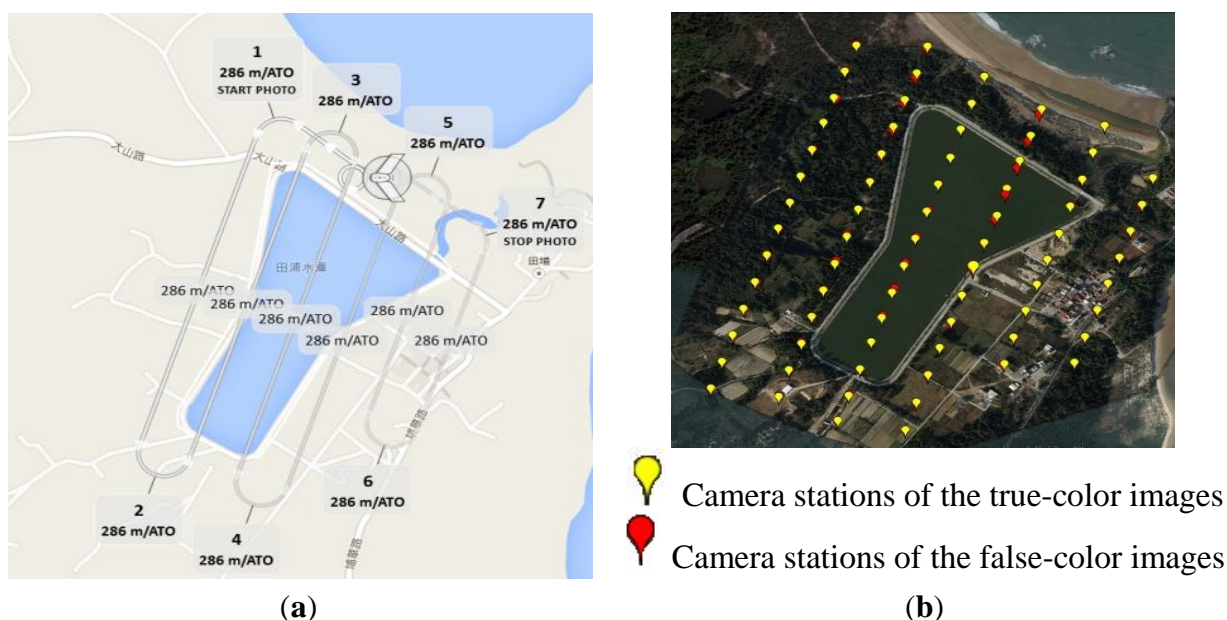


Figure 5. (a) Planned flight path where UAV imaging was started at position 1 and ended at position 7; (b) Locations of 73 schemed camera stations (single flight).

3.4. Image Pre-Processing

The application of UAV imagery to pattern recognition involves the technologies of aerial photogrammetry and remote sensing. The science of optics can be distinguished into geometric and physical optics in the field of aerial photogrammetry and remote sensing, respectively. In geometric optics,

light is considered to travel from a point source through a transmitting medium in straight lines called light rays [32]. Due to the extremely small region of the UAV imaging, atmospheric refraction and the effect of the earth's curvature are ignored. Thus, the UAV image pre-processing in the field of aerial photogrammetry includes correction for lens distortion, aerial triangulation, and ortho-image creation. Photogrammetry software, called Menci Software, was employed in the UAV image pre-processing. Radial, as well as eccentric, lens distortions of the Canon S110 sensors were simultaneously corrected by the Menci Software during aerial triangulation. Finally, the pre-processing result is a mosaic ortho-image and shown in RGB, as in Figure 1.

In physical optics, light is considered as a series of electromagnetic waves traveling through a transmitting medium, such as air [32]. Reflected electromagnetic energies from earth surface features are transformed into spectral response patterns by charge-coupled devices (CCD) in remote sensing sensors. Atmospheric and geometric influences on spectral response patterns are important considerations [33]. Atmospheric influence means that the electromagnetic energy recorded by a sensor is always modified to some extent by the atmosphere between the sensor and the earth's surface. Many applications of satellite remote sensing data entail corrections for the atmospheric path radiance in the spectral bands [6,8–10,34]. Michaelsen & Meidow [17] indicated that their UAV images at 600 m altitude have lower contrast than the virtual globe pictures, probably due to atmospheric effects. However, the altitudes (usually between 100 and 600 m) of the UAVs are not to be compared with those (usually between 800,000 and 900,000 m) of the satellites, so that the atmospheric influence on UAV imagery was limited [35], and therefore ignored, in this research.

Geometric influence, in which reflected electromagnetic energy is primarily a function of the surface roughness of the object, includes the characteristics of specular, near-specular, near-diffuse and diffuse reflectors [33]. In this research, specular reflection was a concern because the body of water in Tain-Pu reservoir would manifest mirror-like reflections, where the angle of reflection equals the angle of incidence. Avoiding the effect of mirror-like reflections is also important for the acquisition of the UAV imagery. We suggest that UAV imaging time should possibly avoid midday operation from 11 a.m. to 1 p.m.

3.5. Establishment of Regression Models

Regression models are established to find the optimal correlations between the water quality parameters and the best band or band ratio. When monitoring water quality, the general methods to find the best band combination include using the ratio between NIR and red bands, or red and blue bands [8,36–40]. Tebbs *et al.* [41] found that Landsat ETM+ band ratio 4/3 gave the best correlation with *in-situ* Chl-a measurements higher than 800 $\mu\text{g L}^{-1}$. Matthews [42] reviewed a large number of studies using Landsat to retrieve SD and found that band ratio 3/1 is particularly common to estimate lake water clarity. Sriwongsitanon *et al.* [43] investigated the relationships between $\ln(\text{SD})$ versus the band ratios of Landsat TM1, TM2, TM3, and TM4 and found that the band ratio 3/1 shows a uniformly high correlation to $\ln(\text{SD})$. Bonansea *et al.* [10] suggested that Landsat band 1 (0.45–0.52 nm), band 4 (0.76–0.90 nm) and band ratio 4/1 show strong negative association with SDT. Zhao *et al.* [29] indicated that the differences in band selection to estimate Chl-a or SD may depend on the limnological properties of the water body.

In Table 2, it is seen that the growth of the algae in Tain-Pu reservoir might be stimulated by TP to increase the concentration of Chl-a and deteriorate the SD. Chlorophyll absorbs energy in the wavelength bands at about 0.45 (blue energy) and 0.67 (red energy) μm , but strongly reflects energy in the wavelength bands of NIR [33]. This paper hypothesizes that the great reflectance difference between the red and NIR bands is useful to detect the concentrations of Chl-a and TP. As for the SD estimation, the ratios between NIR and red bands, blue and red bands, and blue and NIR bands were tested to find the best band combination. According to Sriwongsitanon *et al.* [43], a linear regression model between the log-transformed water quality parameters and band ratios is adopted and described as

$$\ln(\mathbf{Y}) = a \times \ln(\mathbf{X}) + b \quad (1)$$

where \mathbf{X} is the band ratio, \mathbf{Y} denotes water quality parameter, and a and b express coefficient and bias, respectively.

When establishing regression models, it is noticed that single pixel values could not be compared with a ground sample because of water fluidity [6]. Some experts took the 3×3 [2] or 5×5 [6] pixel windows to calibrate image data by averaging the values within the pixel windows. In addition to the average method, we propose a novel method referred to as matching pixel by pixel (MPP), where a 5×5 pixel window is also employed not only to offer an extremely high correlation between band ratio and water quality parameter, but also to precisely determine the corresponding pixel(s) of water quality parameters within the pixel window. Each sampling point is given an individual pixel window corresponding to the on-site area of $50 \times 50 \text{ cm}^2$. Hence, a solution space of $5 \times 5 \times 5$ cube (5×5 pixel window $\times 5$ sampling points) is built for a regression model search; 9,765,625 ($(5 \times 5)^5$) candidate correlations within the solution space can be listed by an enumeration algorithm. Finally, the 9,765,625 candidate correlations are sorted according to their Pearson coefficients to find the optimal correlation.

3.6. Trophic State Mapping

In order to show the trophic state of Tain-Pu reservoir, the predicted concentrations of the water quality parameters of all pixels in the UAV imagery were projected onto the maps with a color bar. Based on the trophic state maps, a brief proposal for management planning of Tain-Pu reservoir is discussed in this paper.

4. Results of Regression Model Establishment and Trophic State Mapping

After producing the ortho-multispectral image, the average and MPP methods were applied to the establishment of regression models. The results of the regression model establishment and trophic state mapping are presented as follows.

4.1. Establishment of Regression Models by the Average Method

A $n \times n$ pixel window is taken into consideration in the average method. The n values, including 5, 9, 19, 49, and 99, were tested to average the reflectance values within the on-site areas of 0.5×0.5 , 1×1 , 2×2 , 5×5 , and $10 \times 10 \text{ m}^2$, respectively. The correlation analysis results between $\ln(\text{NIR}/R)$ and either $\ln(\text{Chl-a})$ or $\ln(\text{TP})$ are shown in Table 4. The positive Pearson coefficients r are consistent

with our expectations, and the average method using the 99×99 pixel windows led to the optimal regression models, where the 59.0% $\ln(\text{Chl-a})$ and 48.7% $\ln(\text{TP})$ can be explained by the $\ln(\text{NIR/R})$.

Table 5 lists the correlation analysis results between $\ln(\text{SD})$ and either $\ln(\text{NIR/R})$, $\ln(\text{R/B})$ or $\ln(\text{NIR/B})$; it is seen that the obtained correlations are positive between $\ln(\text{SD})$ and $\ln(\text{NIR/R})$, but negative between $\ln(\text{SD})$ and $\ln(\text{NIR/B})$. If we ignore the influences of the unconsidered water quality parameters, such as total suspended sediments, *etc.* on SD, a negative correlation is expected, while algae is considered as the unique factor influencing SD. Unfortunately, 0.759 is the highest Pearson coefficient in Table 5, but the positive correlation is inconsistent with our hypothesis. Among the negative correlations, while the Pearson coefficient of -0.445 (between $\ln(\text{SD})$ and $\ln(\text{R/B})$) is optimal, it only explains 19.8% of SD.

A ground area covered by the largest pixel window, *i.e.*, the 99×99 , is approximately equal to that covered by one pixel of satellite imagery, so the UAV imagery has a much smaller minimum mapping unit than the satellite imagery. However, transforming the values within a pixel window into a single averaged value may involve a mixed pixel problem that would hamper the establishing regression model. In Table 5, for example, the larger pixel windows might suffer from the greater influence of mixed pixels than the smaller pixel windows, leading to the lower correlations between the log-transformed band ratios and the SD.

Table 4. Correlation analysis results between $\ln(\text{NIR/R})$ and either $\ln(\text{Chl-a})$ or $\ln(\text{TP})$ using the average method.

<i>n</i>	Y = Chl-a, X = NIR/R			Y = TP, X = NIR/R		
	<i>r</i>	<i>r</i> ²	<i>P</i> value	<i>r</i>	<i>r</i> ²	<i>P</i> value
5	0.405	0.164	0.499	0.573	0.328	0.313
9	0.253	0.064	0.681	0.481	0.231	0.412
19	0.513	0.263	0.377	0.610	0.372	0.275
49	0.487	0.237	0.405	0.573	0.328	0.312
99	0.768	0.590	0.129	0.698	0.487	0.190

Notes: *r* expresses Pearson coefficient; The *P* values were obtained by a two-tail test.

Table 5. Correlation analysis result between $\ln(\text{SD})$ and either $\ln(\text{NIR/R})$, $\ln(\text{R/B})$ or $\ln(\text{NIR/B})$, using the average method.

<i>n</i>	Y = SD, X = NIR/R			Y = SD, X = R/B			Y = SD, X = NIR/B		
	<i>r</i>	<i>r</i> ²	<i>P</i> value	<i>r</i>	<i>r</i> ²	<i>P</i> value	<i>r</i>	<i>r</i> ²	<i>P</i> value
5	0.759	0.576	0.137	-0.445	0.198	0.452	-0.218	0.048	0.725
9	0.423	0.179	0.478	-0.419	0.176	0.482	-0.405	0.164	0.498
19	0.245	0.060	0.692	-0.334	0.112	0.582	-0.275	0.076	0.655
49	0.222	0.049	0.720	-0.338	0.114	0.579	-0.318	0.101	0.602
99	-0.015	0.000	0.980	-0.243	0.059	0.694	-0.222	0.049	0.719

Notes: *r* expresses Pearson coefficient; The *P* values were obtained by a two-tail test.

4.2. Establishment of Regression Models by the MPP Method

The 5 × 5 pixel window was also taken into consideration in the MPP method to find the optimal correlations between the log-transformed band ratios and water quality parameters. Simultaneously, the MPP method was used to determine the corresponding pixel $P_{ij}(m)$ of the water quality parameter, where i and j mean the number of the pixels in the row and column directions of the m^{th} pixel window, respectively; m means the number of the sampling points. In this research, i , j , and m all range from 1 to 5 in integer discreteness.

Table 6 lists the optimal correlations as well as regression coefficients among the 9,765,625 candidate regression models obtained by the MPP method. Except the regression model between $\ln(SD)$ and $\ln(R/B)$, the others have the extremely-high correlation explanations. Compared with NIR/R and NIR/B, NIR/B ($r^2=0.998$) has a little higher explanation than NIR/R ($r^2=0.963$) to SD. As a result, the determined regression models for the optimal predictions of Chl-a, TP, and SD are shown as:

$$\ln(\text{Chl-a}) = 1.0814\ln(\text{NIR/R}) + 5.0176 \text{ for Chl-a prediction} \tag{2}$$

$$\ln(\text{TP}) = 0.7118\ln(\text{NIR/R}) + 4.5720 \text{ for TP prediction} \tag{3}$$

$$\ln(\text{SD}) = -2.0054\ln(\text{NIR/B}) + 0.6414 \text{ for SD prediction} \tag{4}$$

Based on Table 6, the proposed MPP method demonstrated that it is useful for establishing the regression models between the spectral information and the water quality parameters in spite of the limited sampling points. Table 7 shows the most appropriate spectral reflectance values, as well as the corresponded pixels $P_{ij}(m)$ of the five sampling points for each of the above regression models. In the m^{th} 5 × 5 pixel window, the multiple pixels of P_{ij} signify that the pixels have the same band ratio. The 5 × 5 pixel window has demonstrated that it can assist the MPP method in searching for the most appropriate pixel(s) $P_{ij}(m)$ within a neighborhood area of 50 × 50 cm² of a sampling point. In addition, we found that the concentration variation of the water quality parameters can be precisely detected by the least graduations of 0.01 of the log-transformed band ratios.

Table 6. Optimal correlation and regression coefficients obtained by the MPP method, coupled with a 5 × 5 pixel window.

X	Y	Correlation Coefficient			Regression Parameters	
		<i>r</i>	<i>r</i> ²	<i>P</i> value	<i>a</i>	<i>b</i>
	Chl-a	1.000 **	1.000	0.000	1.0814	5.0176
NIR/R	TP	0.999 **	0.997	0.000	0.7118	4.5720
	SD	−0.982 **	0.963	0.003	−4.0138	1.1759
NIR/B	SD	−0.999 **	0.998	0.000	−2.0054	0.6414
R/B	SD	−0.823	0.677	0.087	−1.7424	0.3562

Notes: *r* expresses Pearson coefficient; The *P* values were obtained by a two-tail test; ** denotes the significance at the level of 0.01.

Table 7. Elements $P_{ij}(m)$ corresponding to optimal regression models obtained by the MPP method.

Regression Model	$P_{ij}(m)$									
	$m = 1$		$m = 2$		$m = 3$		$m = 4$		$m = 5$	
	i	j	i	j	i	j	i	j	i	j
<hr/>										
$\ln(\text{Chl-a}) = 1.0814\ln(\text{NIR/R}) + 5.0176$										
(NIR = 34, R = 30, if $m = 1$)										
(NIR = 35, R = 29, if $m = 2$)	1	3								
(NIR = 35, R = 31, if $m = 3$)	2	2	2	4	5	5	4	2	4	5
(NIR = 34, R = 33, if $m = 4$)	3	3					5	2	5	3
(NIR = 37, R = 32, if $m = 5$)										
<hr/>										
					1	1				
					2	1				
					2	5				
					3	1				
$\ln(\text{TP}) = 0.7118\ln(\text{NIR/R}) + 4.5720$					3	2				
(NIR = 35, R = 31, if $m = 1$)	1	1			3	4				
(NIR = 36, R = 29, if $m = 2$)	4	1			3	4	4	2		
(NIR = 35, R = 30, if $m = 3$)	4	2	3	3	4	1	5	2	2	2
(NIR = 34, R = 33, if $m = 4$)	4	3			4	2				
(NIR = 35, R = 30, if $m = 5$)	4	4			4	3				
					4	4				
					5	1				
					5	2				
					5	4				
<hr/>										
$\ln(\text{SD}) = -2.0054\ln(\text{NIR/B}) + 0.6414$										
(NIR = 35, B = 34, if $m = 1$)										
(NIR = 36, B = 33, if $m = 2$)										
(NIR = 35, B = 36, if $m = 3$)	4	4	3	3	2	5	1	2	5	2
(NIR = 37, B = 33, if $m = 4$)					5	5				
(NIR = 36, B = 34, if $m = 5$)										

4.3. Trophic State of Tain-Pu Reservoir

Comparing the regression models obtained by the average with MPP methods (see Tables 4–6), the MPP method can realize the better regression models than the average method. Based on Equations (2) through (4), the log-transformed band ratios of all pixels in the UAV imagery were transformed into the log-transformed water quality parameters, which were recomputed into the exponential values to predict the water quality parameters.

Figure 6 shows the concentration maps of the water quality parameters of Tain-Pu reservoir on 24 November 2014. Figure 6a–c were produced according to the exponential values that resulted from Equations (2)–(4), respectively. The maps in Figure 6 indicate that the low concentrations of Chl-a (less than $140 \mu\text{g}\cdot\text{L}^{-1}$) or TP (less than $100 \mu\text{g}\cdot\text{L}^{-1}$) were mostly distributed over the central part of Tain-Pu reservoir, near sampling point 3 (see Figure 1). However, the high concentrations of Chl-a (between 140 and $260 \mu\text{g}\cdot\text{L}^{-1}$) or TP (between 100 and $140 \mu\text{g}\cdot\text{L}^{-1}$) were mostly distributed over the region involving sampling point 2, which is also the traditional sampling point of the Environmental Protection Bureau, Kinmen.

Among the predicted water quality parameters, some values are either extremely higher or lower than the others, e.g., the Chl-a concentrations over $103 \mu\text{g}\cdot\text{L}^{-1}$, or the SD depths under 10^{-2} m.

Figure 7 marks the extreme values of the water quality parameters using the yellow elements. We can see that the extreme values exist approximately on the edge between the water body and land, or are distributed over the southwest side of Tain-Pu reservoir. Most of the predicted SD depths on the edge between water body and land are under 10^{-2} m, which is reasonable due to the shore-line. On the contrary, the extremely low SD depths would correspond to the extremely high Chl-a or TP concentrations so that the predicted Chl-a or TP values are extraordinary. The sawtooth region of the extreme values over the southwest side of Tain-Pu reservoir resulted from the shadow of the neighboring forest. We see that the SD depths in the sawtooth region are above 3 m, even up to 25 m. However, the above SD depths are clearly unreasonable because the average depth of Tain-Pu reservoir is about 3.4 m. Additionally, the predicted Chl-a or TP concentrations in the sawtooth region are extraordinary and should be ignored. Conclusively, the regular values of Chl-a, TP, and SD might be between 100 and $300 \mu\text{g}\cdot\text{L}^{-1}$, 80 and $160 \mu\text{g}\cdot\text{L}^{-1}$, and 0.5 and 3.0 m, respectively. Except for the extreme values, the average water quality parameters were calculated, as shown in Figure 6. According to the Carlson TSI [31], this paper demonstrates that the trophic state of Tain-Pu reservoir is hypereutrophic.

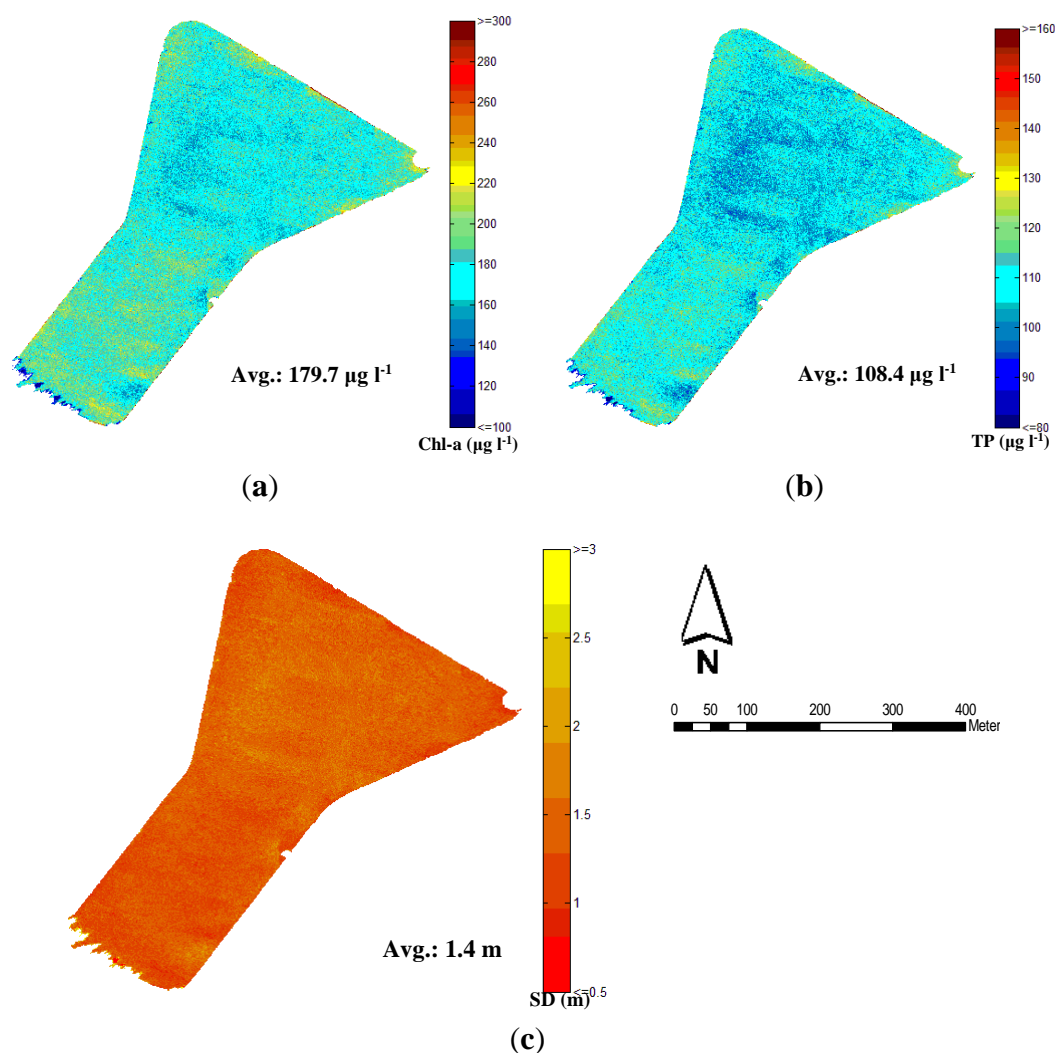


Figure 6. Concentration maps of water quality parameters of Tain-Pu reservoir on 24 November 2014: (a) Chl-a concentration map; (b) TP concentration map; (c) SD depth map.

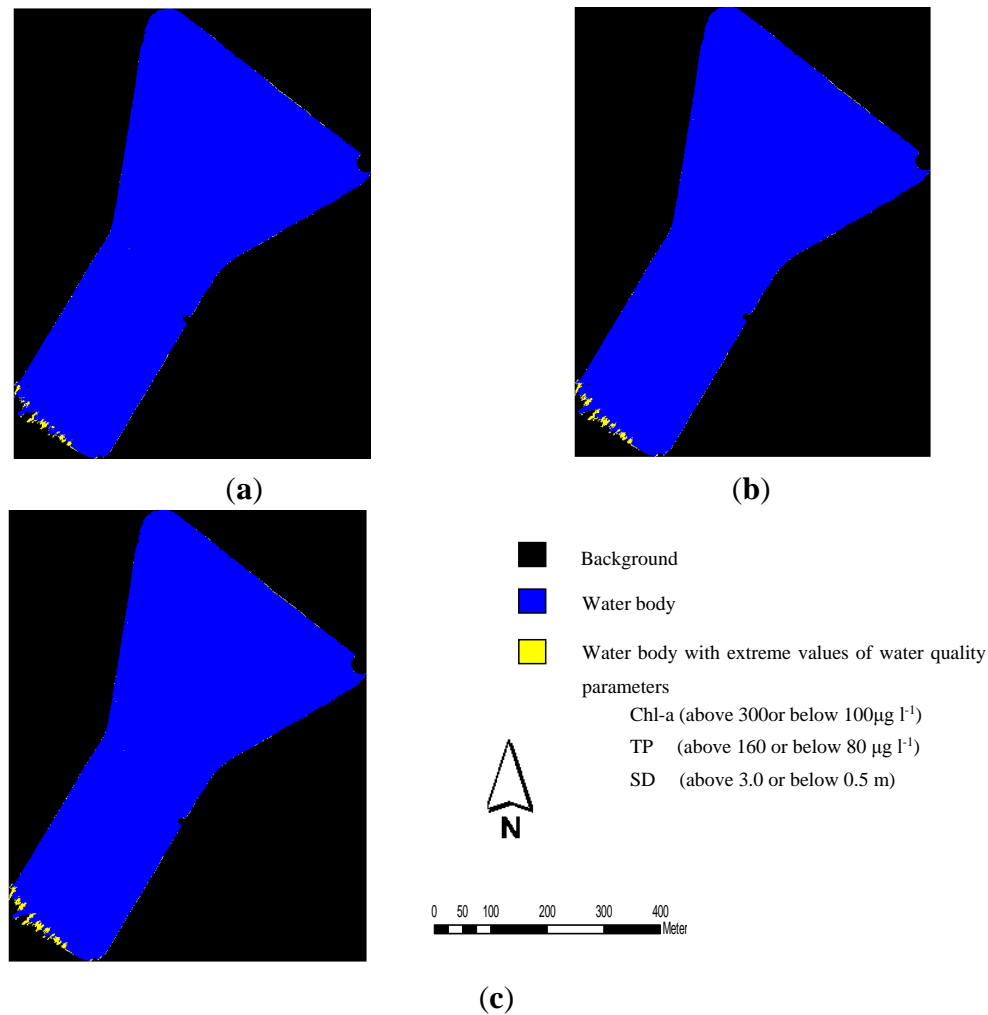


Figure 7. Mapping for extreme values of water quality parameters: (a) Chl-a, (b) TP, (c) SD.

5. Discussion

The acquired UAV imagery was geo-referenced to the coordinate system of GCS_TWD_1997 so that the thematic maps of the trophic state can be overlaid with the other spatial data, such as land use, population, groundwater, *etc.*, in the GIS environment to carry out an overlay analysis. The other 11 small reservoirs in Kinmen will also provide their thematic maps of trophic states in the future. By the overlay analysis, the critical factors affecting water resource fragility could be determined for the sustainable planning of Kinmen. Referring to the trophic state mapping in Figure 6, a brief proposal for management planning of Tain-Pu reservoir is described as follows:

- Figure 6 shows that the higher concentrations of Chl-a or TP are distributed over the southwest side of Tain-Pu reservoir. Compared to the historical data of Chl-a and TP in the fall (see Table 1), with their examination data at sampling point 2 (see Table 3), *i.e.*, the traditional sampling point, the concentrations of Chl-a and TP were significantly higher in the past years. We conjecture that the problem results from the current stream regulation project on the southwest side of Tain-Pu reservoir blocking the upstream water from flowing into the reservoir. Once the stream regulation project is finished, reinforcing the circulation of the water body is extremely important.

- 2 Due to the hypereutrophic state of Tain-Pu reservoir, the current water body should be totally drained from the reservoir before receiving potable water from China. Simultaneously, the pollutant sources should be entirely surveyed and controlled to ensure that the reservoir has the capacity for self-oxidation.

The multispectral UAV imagery with the extremely-high spatial resolution of 0.1 m is useful to assist the MPP method in searching the robust regression models. Moreover, the fine spatial resolution offers good concentration contrast for the small reservoir. In addition to Kinmen, we would like to greatly promote our UAV imaging technique and MPP method to be applied to water quality monitoring of small reservoirs in other small islands around the world, especially for Hong Kong or Macau, as both city islands of mainland China have an extreme high population density but, similarly, need to rely on the potable water supply of mainland China.

Among the band ratios of NIR/R, NIR/B, and R/B, the MPP method demonstrates that NIR/R and NIR/B have the best correlation with either Chl-a or TP and SD, respectively, so that the amount of algae would have a critical impact on the transparency of Tain-Pu reservoir. In spite of this, it is noticed that the obtained regression models may lead to an excessive optimization. Thus, a regression with observed data and predicted data should be calculated. However, the current observed data are obviously insufficient for the regression calculation. A multi-temporal water quality monitoring of Tain-Pu reservoir should be implemented for observed data accumulation. In each monitoring work, we will scheme more than five sampling points in order to assess the adjustments based on the redundant observed data. While assessing the adjustments, however, it is difficult to accurately identify pixels of spectral reflectance corresponding to the observed data because of the fine spatial resolution and water fluidity. This paper proposes that, prior to the adjustment assessment, the different number of sampling points should be taken into consideration in the MPP method to determine the variation of obtained Pearson coefficients and r^2 values.

6. Conclusions

The total cost of the processes, including measurement, *in situ*, water quality exam, UAV imaging, and image processing, is about \$5000 USD. After measurement, *in situ*, and UAV imaging, the duration needed from water quality exam to trophic state mapping is about two weeks. In this case study, the fine temporal resolution and mobility of UAV demonstrated that they could effectively preclude the weather from harming the aerial imaging. Thus, compared with the traditional techniques of photogrammetry or satellite remote sensing, UAVs offer a better ratio between cost and profit in the trophic state mapping of small reservoirs. The proposed UAV imaging technique could be widely applied to water quality monitoring for the small reservoirs/lakes in other small islands around the world.

Establishing the appropriate regression models is usually difficult for the application of remote sensing data to monitoring water quality. This research presented the MPP method, a novel method for establishing a regression model, and compared the performances of the MPP method with the traditional average method. The experimental result shows that the MPP method can lead to an extremely high Pearson coefficient (r^2 approximating to 1.0). Based on the regression models obtained by the MPP method, Chl-a and TP have positive correlations with the band ratio of NIR/R, and SD has a negative correlation with the band ratio of NIR/B. Consequently, the concentrations of the water

quality parameters in Tain-Pu reservoir should be principally controlled by the algae amount in the water body.

In Tain-Pu reservoir, the predicted regular values of Chl-a, TP, and SD might be between 100 and 300 $\mu\text{g L}^{-1}$, 80 and 160 $\mu\text{g L}^{-1}$, and 0.5 and 3.0 m, respectively. The averages of Chl-a, TP, and SD are 179.7 $\mu\text{g L}^{-1}$, 108.4 $\mu\text{g L}^{-1}$, and 1.4 m, respectively. According to the Carlson TSI [31], the trophic state of Tain-Pu reservoir is hypereutrophic. However, the characteristic of the small reservoirs in Kinmen is absolutely different from that in North America. An appropriate TSI for describing the trophic states of the small reservoirs in Kinmen should be studied.

At present this research only produces the trophic state maps of Tain-Pu reservoir for the water quality monitoring of a single period, but a water quality monitoring of multiple periods is expected in the future. Additionally, the proposed technique should be applied to the water quality monitoring for the other small reservoirs in Kinmen so that the water resource fragility and sustainable planning in Kinmen can be discussed. If the 5×5 pixel window cannot assist the MPP method in establishing a regression model with an acceptable Pearson coefficient, the size of the pixel window is suggested to be appropriately enlarged. However, it was noticed that the larger the pixel window is, the longer the needed computation time.

Acknowledgments

This research was performed within the framework of the project “Analysis of Environmental Fragility and Studies on Sustainable Planning for Small Islands: Water Resource Issues (II)”, funded by the Ministry of Science and Technology, Taiwan (MOST 103-2621-M-507-001-).

Author Contributions

Tung-Ching Su organized this research, acquired the exam data of the water quality parameters, presented and executed the MPP method, produced the trophic state maps, analyzed the experimental results, and finally wrote this manuscript. Hung-Ta Chou was in charge of the UAV imaging and the image pre-processing.

Conflicts of Interest

The authors declare no conflict of interest.

References

1. Lillesand, T.M.; Johnson, W.L.; Deuell, R.L.; Lindstrom, O.M.; Meisner, D.E. Use of Landsat data to predict the trophic state of Minnesota Lakes. *Photogramm. Eng. Remote Sens.* **1983**, *49*, 219–229.
2. Giardino, C.; Pepe, M.; Brivio, P.A.; Ghezzi, P.; Zilioli, E. Detecting chlorophyll, Secchi disk depth and surface temperature in a sub-alpine lake using Landsat imagery. *Sci. Total Environ.* **2001**, *268*, 19–29.
3. Vos, R.J.; Hakvoort, J.H.M.; Jordans, R.W.; Ibelings, B.W. Multiplatform optical monitoring of eutrophication in temporally and spatially variable lakes. *Sci. Total Environ.* **2003**, *312*, 221–243.

4. Erkkilä A.; Kalliola, R. Patterns and dynamics of coastal waters in multi-temporal satellite images: Support to water quality monitoring in the Archipelago Sea, Finland. *Estuar. Coast. Shelf Sci.* **2004**, *60*, 165–177.
5. Sass, G.Z.; Creed, I.F.; Bayley, S.E.; Devito, K.J. Understanding variation in trophic status of lakes on the Boreal Plain: A 20year retrospective using Landsat TM imagery. *Remote Sens. Environ.* **2007**, *109*, 127–141.
6. Wang, Y.; Xia, H.; Fu, J.; Sheng, G. Water quality change in reservoirs of Shenzhen, China: Detection using LANDSAT/TM data. *Sci. Total Environ.* **2004**, *328*, 195–206.
7. Chen, L.; Tan, C.H.; Kao, S.J.; Wang, T.S. Improvement of remote monitoring on water quality in a subtropical reservoir by incorporating grammatical evolution with parallel genetic algorithms into satellite imagery. *Water Res.* **2008**, *42*, 296–306.
8. Wang, Z.; Hong, J.; Du, G. Use of satellite imagery to assess the trophic state of Miyun Reservoir, Beijing, China. *Environ. Pollut.* **2008**, *155*, 13–19.
9. Schroeter, L.; Gläßer, C. Analyses and monitoring of lignite mining lakes in Eastern Germany with spectral signatures of Landsat TM satellite data. *Int. J. Coal Geol.* **2011**, *86*, 27–39.
10. Bonansea, M.; Rodriguez, M.C.; Pinotti, L.; Ferrero, S. Using multi-temporal Landsat imagery and linear mixed models for assessing water quality parameters in Ró Tercero reservoir (Argentina). *Remote Sens. Environ.* **2015**, *158*, 28–41.
11. Palmer, S.C.J.; Kutser, T.; Hunter, P.D. Remote sensing of inland waters: Challenges, progress and future directions. *Remote Sens. Environ.* **2015**, *157*, 1–8.
12. Yang, M.D.; Sykes, R.M.; Merry, C.J. Estimation of algal biological parameters using water quality modeling and SPOT satellite data. *Ecol. Model.* **2000**, *125*, 1–13.
13. Dekker, A.G.; Vos, R.J.; Peters, S.W.M. Analytical algorithms for lake water TSM estimation for retrospective analyses of TM and SPOT sensor data. *Int. J. Remote Sens.* **2002**, *23*, 15–35.
14. Tarrant, P.E.; Amacher, J.A.; Neuer, S. Assessing the potential of Medium-Resolution Imaging Spectrometer (MERIS) and Moderate-Resolution Imaging Spectroradiometer (MODIS) data for monitoring total suspended matter in small and intermediate sized lakes and reservoirs. *Water Resour. Res.* **2010**, *46*, doi:10.1029/2009WR008709.
15. Olmanson, L.G.; Brezonik, P.L.; Bauer, M.E. Evaluation of medium to low resolution satellite imagery for regional lake water quality assessments. *Water Resour. Res.* **2011**, *47*, doi:10.1029/2011WR011005.
16. Huang, C.; Wang, X.; Yang, H.; Li, Y.; Wang, Y.; Chen, X.; Xu, L. Satellite data regarding the eutrophication response to human activities in the plateau lake Dianchi in China from 1974 to 2009. *Sci. Total Environ.* **2014**, *485–486*, 1–11.
17. Michaelsen, E.; Meidow, J. Stochastic reasoning for structural pattern recognition: An example from image-based UAV navigation. *Pattern Recognit.* **2014**, *47*, 2732–2744.
18. Niethammer, U.; James, M.R.; Rothmund, S.; Travelletti, J.; Joswig, M. UAV-based remote sensing of the Super-Sauze landslide: Evaluation and results. *Eng. Geol.* **2012**, *128*, 2–11.
19. Zarco-Tejada, P.J.; González-Dugo, V.; Berni, J.A.J. Fluorescence, temperature and narrow-band indices acquired from a UAV platform for water stress detection using a micro-hyperspectral imager and a thermal camera. *Remote Sens. Environ.* **2012**, *117*, 322–337.

20. Zarco-Tejada, P.J.; Guillen-Climent, M.L.; Hernandez-Clemente, R.; Catalina, A.; Gonzalez, M.R.; Martin, P. Estimating leaf carotenoid content in vineyards using high resolution hyperspectral imagery acquired from an unmanned aerial vehicle (UAV). *Agric. Forest Meteorol.* **2013**, *171–172*, 281–294.
21. Colomina, I.; Molina, P. Unmanned aerial systems for photogrammetry and remote sensing: A review. *ISPRS J. Photogramm. Remote Sens.* **2014**, *92*, 79–97.
22. Immerzeel, W.W.; Kraaijenbrink, P.D.A.; Shea, J.M.; Shrestha, A.B.; Pellicciotti, F.; Bierkens, M.F.P.; de Jong, S.M. High-resolution monitoring of Himalayan glacier dynamics using unmanned aerial vehicles. *Remote Sens. Environ.* **2014**, *150*, 93–103.
23. Peter, K.D.; d'Oleire-Oltmanns, S.; Ries, J.B.; Marzloff, I.; Hssaine, A.A. Soil erosion in gully catchments affected by land-levelling measures in the Souss Basin, Morocco, analysed by rainfall simulation and UAV remote sensing data. *Catena* **2014**, *113*, 24–40.
24. Torres-Sanchez, J.; Pena, J.M.; de Castro, A.I.; Lopez-Granados, F. Multi-temporal mapping of the vegetation fraction in early-season wheat fields using images from UAV. *Comput. Electron. Agric.* **2014**, *103*, 104–113.
25. Bendig, J.; Yu, K.; Aasen, H.; Bolten, A.; Bennertz, S.; Broscheit, J.; Gnyp, M.L.; Bareth, G. Combining UAV-based plant height from crop surface models, visible, and near infrared vegetation indices for biomass monitoring in barley. *Int. J. Appl. Earth Obs. Geoinf.* **2015**, *39*, 79–87.
26. Flynn, K.F.; Chapra, S.C. Remote sensing of submerged aquatic vegetation in a shallow non-turbid river using an unmanned aerial vehicle. *Remote Sens.* **2014**, *6*, 12815–12836.
27. Pajares, G. Overview and current status of remote sensing applications based on unmanned aerial vehicles (UAVs). *Photogramm. Eng. Remote Sens.* **2015**, *81*, 281–330.
28. Pavluk, T.; bij de Vaate, A. Trophic index and efficiency. In *Encyclopedia of Ecology*; Jorgensen, S.E., Fath, B., Eds.; Elsevier: Amsterdam, The Netherlands, 2008; pp. 3602–3608.
29. Zhao, D.; Cai, Y.; Jiang, H.; Xu, D.; Zhang, W.; An, S. Estimation of water clarity in Taihu Lake and surrounding rivers using Landsat imagery. *Adv. Water Resour.* **2011**, *34*, 165–173.
30. Environmental Analysis Laboratory, EPA, Taiwan. Available online: <http://www.niea.gov.tw/analysis/method/ListMethod.asp?methodtype=LIVE> (accessed on 28 June 2015).
31. Carlson, R.E. A trophic state index for lakes. *Limnol. Oceanogr.* **1997**, *22*, 361–369.
32. Wolf, P.R.; Dewitt, B.A. *Elements of Photogrammetry with Applications in GIS*, 3rd ed.; McGraw-Hill: Taipei, Taiwan, 2000.
33. Lillesand, T.M.; Kiefer, R.W.; Chipman, J.W. *Remote Sensing and Image Interpretation*, 6th ed.; Wiley: NJ, USA, 2008.
34. Doña, C.; Chang, N.B.; Caselles, V.; Sánchez, J.M.; Camacho, A.; Delegido, J.; Vannah, B.W. Integrated satellite data fusion and mining for monitoring lake water quality status of the Albufera de Valencia in Spain. *J. Environ. Manag.* **2015**, *151*, 416–426.
35. Zaman, B.; Jensen, A.; Clemens, S.R.; McKee, M. Retrieval of spectral reflectance of high resolution multispectral imagery acquired with an autonomous unmanned aerial vehicle: AggieAir™. *Photogramm. Eng. Remote Sens.* **2014**, *80*, 1139–1150.

36. Chipman, J.W.; Olmanson, L.G.; Gitelson, A.A. *Remote Sensing Methods for Lake Management: A Guide for Resource Managers and Decision-Makers*; Developed by the North American Lake Management Society in Collaboration with Dartmouth College, University of Minnesota, and University of Nebraska, for the United States Environmental Protection Agency: Madison, WI, USA, 2009.
37. Kloiber, S.M.; Brezonik, P.L.; Olmanson, L.G.; Bauer, M.E. Application of Landsat imagery to regional-scale assessments of lake clarity. *Water Res.* **2002**, *36*, 4330–4340.
38. Chipman, J.W.; Lillesand, T.M.; Schmaltz, J.E.; Leale, J.E.; Nordheim, M.J. Mapping lake clarity with Landsat images in Wisconsin, U.S.A. *Can. J. Remote Sens.* **2004**, *30*, 1–7.
39. Olmanson, L.G.; Bauer, M.E.; Brezonik, P.L. A 20-year Landsat water clarity census of Minnesota's 10,000 lakes. *Remote Sens. Environ.* **2008**, *112*, 4086–4097.
40. McCullough, I.M.; Loftin, C.S.; Sader, S.A. High-frequency remote monitoring of large lakes with MODIS 500 m imagery. *Remote Sens. Environ.* **2012**, *124*, 234–241.
41. Tebbs, E.J.; Remedios, J.J.; Harper, D.M. Remote sensing of chlorophyll-a as a measure of cyanobacterial biomass in Lake Bogoria, a hypertrophic, saline–alkaline, Flamingo Lake, using Landsat ETM+. *Remote Sens. Environ.* **2013**, *135*, 92–106.
42. Matthews, M.W. A current review of empirical procedures of remote sensing in inland and near-coastal transitional waters. *Int. J. Remote Sens.* **2011**, *32*, 6855–6899.
43. Sriwongsitanon, N.; Surakit, K.; Thianpopirug, S. Influence of atmospheric correction and number of sampling points on the accuracy of water clarity assessment using remote sensing application. *J. Hydrol.* **2011**, *401*, 203–220.

© 2015 by the authors; licensee MDPI, Basel, Switzerland. This article is an open access article distributed under the terms and conditions of the Creative Commons Attribution license (<http://creativecommons.org/licenses/by/4.0/>).